On the polarimetric backscatter by a still or quasi-still wind turbine

Marco Gabella[1], Martin Lainer[1], Daniel Wolfensberger[1], Jacopo Grazioli[2]

[1]Federal Office of Meteorology and Climatology MeteoSwiss, Locarno-Monti, CH-6605, Switzerland
[2]Environmental Remote Sensing Laboratory, École polytechnique fédérale de Lausanne, Lausanne, Switzerland

5 *Correspondence to*: Marco Gabella (marco.gabella@meteoswiss.ch)

Abstract.

Wind turbines negatively affect the performance of weather radars, especially when located in the proximity of a radar site. In March 2019, MeteoSwiss performed a measurement campaign by deploying a mobile X-band radar in Schaffhausen. It proved to be useful for mapping and characterizing the maximum power returns by three wind turbines observed using standard
10 scanning strategies. In March 2020, the campaign has been repeated using a more sophisticated scan strategy: ~100-minute special sessions of fixed-pointing antenna towards the nacelle of the closest wind turbine (WT) located at 7766 m range from the radar, interleaved every 2 hours by a scanning protocol identical to the March 2019 campaign. Polarimetric radar signatures have been derived every 64 ms using 128 radar pulses transmitted every 0.5 ms (PRF = 2000 Hz). A thorough overview of the polarimetric signatures of the WT in still or quasi-still conditions has been obtained based on thirty thousand polarimetric
15 measurables acquired during 32 minutes of the first day of the campaign (March 4, 2020). During the first 2 minutes with zero rotor speed, the copolar correlation coefficient between the orthogonal polarization states, ρ_{HV}, was persistently equal to 1, similar to the signature of a Bright Scatterer observed by a non-rotating antenna. The changes between two consecutive values of the differential reflectivity and radar reflectivity factor were either 0 dBz or ±0.5 dBz. Due to the absence of precipitation, one could assume that the standard deviation of the differential phase shift, which was as small as 3.0°, can be entirely attributed
20 to the variability of the differential backscattering phase shift. There were two 10-min periods during which the rotor has moved less than 1 revolution. It is worth noting that this slow movement could be associated to a change in the blade pitch angle and the nacelle orientation, which caused extreme changes in the radar reflectivity factor. For instance, two pairs of 64 ms consecutive values have reached 78.5 dBz, which is the absolute maximum reached in the whole campaign (March 4-21, 2020).

25 **1 Introduction**

Wind turbines can heavily affect sensitive radar applications including weather, surveillance, precision approaching and air traffic control. Furthermore, the operation of air traffic radio navigation systems like VOR (VHF omnidirectional range) can be disturbed by nearby wind turbines (e.g., Morlaas et al., 2008; Douvenot et al., 2017). In 2021 the European countries invested about €41billion in new wind farms, covering 24.6 GW of new capacity (Brindley, 2022). As large as these quantities

1

are, they are still far off from the European goal to reach its new climate change and energy security targets. Consequently, the expected continuous and strengthened expansion of wind farms is of major concern for the weather (e.g., Norin, 2017) and aviation radar community (e.g., Cuadra et al., 2019). Wind turbines are large objects with a variety of movement patterns, which makes them a strong source of clutter that is difficult to filter. Several studies exist in the literature regarding the impact of wind turbines on radar systems. From a weather radar viewpoint, of particular interest are those discussing the issue of contamination of weather radar data (Hood et al., 2010; Angulo et al., 2015; Lepetit et al., 2019); for other sectors, the identification of adverse effects of wind turbines on the performance of air surveillance and marine radars is of great concern (Angulo et al., 2014; Cuadra et al., 2019). In general, the radar reflectivity factor of wind turbine clutter depends on various parameters such as wind turbine dimensions, incidence angle of the radiation, rotor speed, blade pitch angles, nacelle orientation and radiation frequency (Gallardo-Hernando et al., 2011; Norin, 2015; Lainer et al., 2021). In literature, several papers about the radar reflectivity factor (and equivalent backscattering radar cross section) of the wind turbines can be found. One can separate the studies between those dealing primarily with measurements (e.g., Bredemeyer et al., 2019; Kong et al., 2011; Kent et al., 2008) and others using numerical investigations of virtual wind turbine models (e.g., Muñoz-Ferreras et al., 2016; de la Vega et al., 2016).

Published research dealing with other polarimetric signatures of the WT is rare. In a recent (March 4-21, 2020), unique stare mode campaign held in Schaffhausen (Lainer et al., 2021), the WT is continuously illuminated by a fixed-pointing antenna. As emphasized by Reviewer 1 (Interactive comment on *Atmos. Meas. Tech. Discuss*, 2020): "the measurements as they are described provide further information on the properties of other polarimetric variables at the WT location. This information is urgently needed to comprehend the WT problem and I want to encourage the authors to add further publications based on this experiment". This preliminary study represents a small step in the direction of filling such polarimetric gap. However, it is important to point out that our main objective is an investigation of the dual-polarization backscattered signals by a wind turbine (WT) when its rotor speed is very small or even close to zero, as well as during the transition from zero rotor speed to the ordinary moving conditions.

The reason is connected to the emerging interest toward "Bright" Scatterers (BS) (Rinehart, 1978) as additional tool for monitoring modern dual-polarization weather radars (Gabella, 2018). Thanks to the increased number of dual-polarization radars and in computational power for modeling and statistical analysis, a novel point of view regarding ground clutter has emerged. It is no longer considered exclusively a disturbance that needs to be rejected; rather, its spatio-temporal properties are statistically characterized in order to be used for monitoring radar hardware. This is the case of the BS, which is a tall target, close to the radar and hit by the antenna beam axis. It has been recently shown that the "historical" polarimetric and spectral signatures of a BS in Switzerland represent a benchmark for an in-depth comparison after hardware replacements (Gabella, 2021). However, since it is illuminated according to a scan strategy which is optimized for an operational monitoring of the weather (Germann et al., 2022), the typical return period for BS observations is as large as 5 minutes (300 s). Thanks to the recent unique MeteoSwiss stare mode campaign in Schaffhausen (March 4-21, 2020), the WT is continuously illuminated by a fixed-pointing antenna with a large number of pulses ($N = 128$). Using a PRF as large as 2000 Hz, dual-polarization

signatures are available every 64 ms (128/2000). The fixed pointing antenna turns out to be an important advantage, if one aims at characterizing the intrinsic spectral signatures of the large, "bright" target.

A description of the radar with the dedicated scan strategy, the geographical area of operation, and the observed WT is given in Sec. 2.1. Sec. 2.2 presents the WT metadata, which are unfortunately available only every 600 s. Sec. 3 represents the core of this manuscript: Sec. 3.1 shows that the copolar coefficient of a still WT (rotor speed equal to 0) is perfectly stable and equal to 1; the dispersion of both the differential phase shift and the differential reflectivity is small; the values of the radar reflectivity factor for both polarizations also show very small variability. However, Sec. 3.2 shows that the situation becomes completely different when even a small rotation (and/or change in the blade pitch angle or nacelle orientation) takes place. Interestingly, Sec. 3.3 and 3.4 will show that the maxima constructive and destructive interference do not occur in ordinary moving condition (Sec. 3.3, stationary rotations for most of the ten minutes), rather during the small partial, "discontinuous" rotation that took place in the successive ten minutes (Sec. 3.4, a partial rotation of 216˚). A thorough discussion is presented in Sec. 4, conclusions and outlook are found in Sec. 5.

2 Brief description of the experimental area, instrumentation and high temporal resolution data

2.1 The radar site (good visibility towards the wind turbine), observation geometry and the simple scan strategy

A dual-polarization, Doppler, mobile X-band radar has been used for the measurement campaign. A detailed technical overview of the radar system can be found in Neely et al. (2018). Some key specifications are listed in Table 2 of Lainer et al, 2021. The radar was installed near the city of Schaffhausen (approximate coordinates: 47.700° latitude and 8.664° longitude using the WGS84 datum), at an altitude of 455 m. The three wind turbines of the small wind park located north of Schaffhausen are installed on a hill surrounded by forests. For the specifications and other properties (including geometry) of the wind turbines, the reader may refer to Table 1 in Lainer et al. (2021). For the whole campaign in 2020, we observed only the wind turbine with the best visibility and maximum radar reflectivity factor observed during the 2019 campaign. This turbine was indicated as WT1 in Lainer et al. (2021), here after it will be simply labeled as WT. The horizontal distance from its mast and the radar site is 7.76 km. By analyzing the output of the simulations by the X-band Ground Echo Clutter Simulator (GECS-X) described by Gabella et al. (2008), which has been run using a digital elevation model (DEM) with 50m resolution, the radar visibility towards the wind turbines could be determined. The used approach follows the simple but effective geometric optics assumption described in Gabella and Perona (1998). From the "visibility" map (see Fig. 1a in Lainer et al., 2021), one gets the minimum angle of elevation at which a target could be "seen" from the radar site, which is 2.25˚. If no obstacles were present on the surface, then the base of the WT at ~765 m would be visible from the radar site: the nominal angle of elevation using simple trigonometry (and flat Earth) turns to be, in fact, 2.305˚ (see Fig. 1c in Lainer et al., 2021, but at the exact range of 7766 m of the present WT). A wood of conifers is instead present between the radar and the WT: those tall trees, at approximately 1km range, partially block just a small part of the main lobe towards the base of the mast; on the contrary, the rotor center of the WT is always visible: knowing the nacelle height, in fact, it is easy to derive that the angle of elevation of

the rotor center is 3.308˚ (range is ~7773 m). Finally, the angle of elevation for the vertical pointing end of a blade is 3.789 ˚ (range is ~7777 m).

For the distinctive stare-mode strategy of the March 2020 campaign, we have opted for an angle of elevation of 3.1˚: consequently, the whole half power beam width (HPBW, from 2.45 ˚ to 3.75˚, in the elevation plane) is practically not subject to occultation by obstacles. The azimuth was set to 338.9˚. In this study we will present polarimetric signatures derived using I and Q data of Gate103 (starting from 0), which ranges from 7725 m to 7800 m. At such range, the size of the pencil beam HPBW is about 180 m. On the contrary, the range resolution is independent of range: being a priori known at what range the (weather) target should be detected and investigated, it can be pushed down to half the pulse width multiplied by the speed of light. This is in fact the case for our X-band radar with a pulse width of 500 ns (specifications and more details regarding the radar can be found in Table 2 of Lainer et al., 2021). It is then clear that the WT target is thoroughly bounded inside the radar sampling volume of 180 m ×180 m ×75 m (0.0243 km^3) only as long as the nacelle orientation is around 0˚ or 180˚. When the orientation goes toward 90˚ or 270˚, part of the 65 m blades (130 m diameter) will exceed the range resolution. It is also evident that the tall, complex-shape WT cannot be assumed to be a point target, in order to retrieve a value of radar cross section from the measured power, in turn converted into radar reflectivity factor using the Probert-Jones (1962) approximation (Gaussian distribution of the radiated power over the main lobe). If one pretended the point target radar equation (s. e.g., eq. (1) in Lainer et al., 2021) being applicable and compared it with the Probert-Jones meteorological radar equation (s., e.g., eq. (6) in Lainer et al., 2021), then the radar cross section (RCS, expressed in dB square meters) could be derived by simply decreasing by 34.4 dB the radar reflectivity factor (expressed in dBz, see Sec. 2.3.1).

2.2 Wind turbine data and metadata collection: detailed investigation during a 40-minute interval starting and ending with 0 rotor speed

The focus of the present study is limited to dual-polarization backscattered signals in correspondence of a situation with zero rotor speed. Hence, the prerequisite is the presence of a 10 min interval without any rotor rotation. Despite being unusual, this situation has happened on the first day of the campaign, namely between 17:00 and 17:10 UTC on March 4, 2020. We are aware of such special conditions thanks to Hegauwind GmbH & Co. KG Verenafohren that have kindly provided the operational data of the wind turbines. These include environmental (e.g., wind speed, direction, outsidetemperature), instrumental (indoor and hardware temperature, current, voltage, power) and operational (e.g., nacelle direction, rotor speed, pitch angle of the three blades) for a total of almost a hundred parameters. Unfortunately, such abundance of parameters cannot compensate the main limitation of these data, which is their granularity. As a matter of fact, they are available only every 10 minutes, while the high-temporal resolution radar echoes are available every 64 ms. As shown by Lainer et al. (2021), the average rotor speed and the blade pitch angle are by far the most important information for radar-related studies. For instance, zero (or very small) rotor speed is typically associated to a large value of the angle of the 3 blades, as it can be seen in Fig. 1 (red vs blue dots).

During the first 12 hours of the campaign (March 4, 2020), the 10-min average rotor speed was particularly large, ranging from 7 to 11 rpm (blade pitch angle close to 0). But in the second part of the day, which is displayed in Fig. 1, a 4-hour period

130 with an almost constant and regular rotor speed of about 7 rpm has taken place, followed by a quiet period between 16:40 and 17:00 UTC (average rotor speed around 0.1 rpm, red dots; blade pitch angle at 70˚, blue dots). In particular, the conditions during the 17:00-17:10 UTC interval on March 4, 2020 were ideal from our viewpoint: the average rotor speed was exactly 0 rpm, so that we know no movements have happened (the blade pitch angles were also kept constant at 70˚). During the two (final) minutes with available radar data, we will see that radar measurables are very stable with no (or very little) variability.

135 This fact will be investigated and shown at the original very high temporal resolution of 64 ms and displayed using a re-sampled 8 s temporal resolution in Sec. 3.1. The (8 s) low resolution analysis is based on the maximum, minimum and median values of 125 original (64 ms) echoes. The nacelle orientation with respect to the radar beam axis was about 61˚ (see Fig. 3a , Lainer et al., 2021; an orientation of 0˚ means that the nacelle is pointing towards the radar).
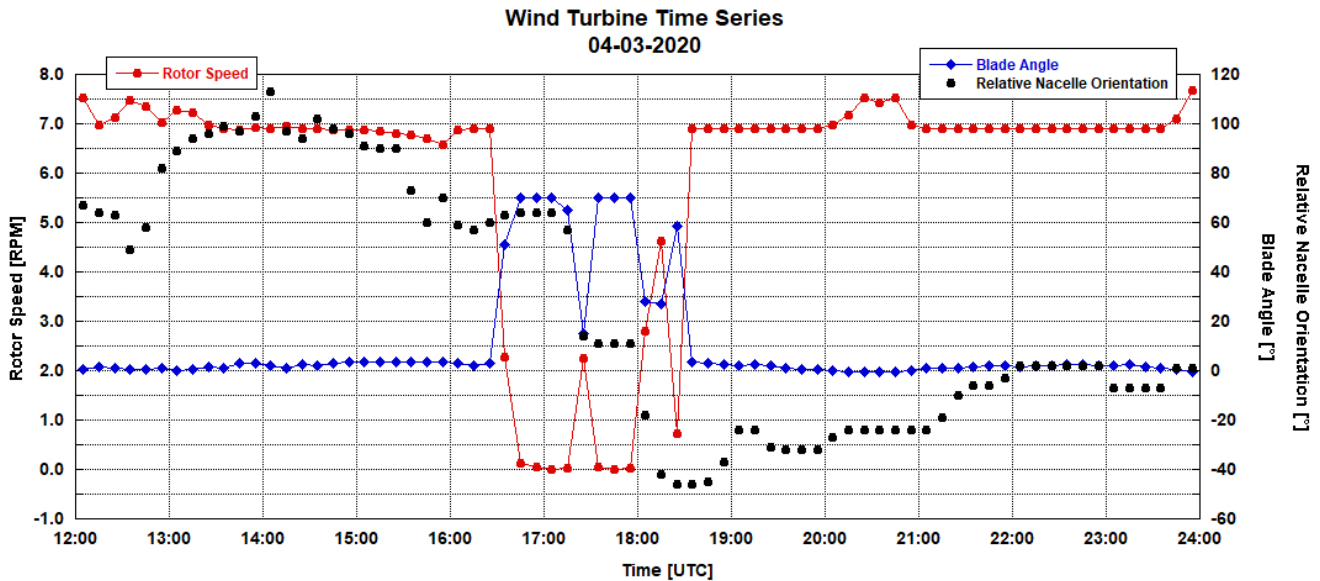
140

Figure 1. Wind turbine rotor speed (red, left y-axis), blade pitch angle (blu, right y-axis), and nacelle orientation (black dots, right y-axis) on March 4, 2020.

The analyses of the successive period $P2$ (17:10-17:20 UTC) will be presented in Sec. 3.2.During $P2$, the blade pitch angles

145 have been reduced from 70˚ to 65˚ (see Fig. 1, blue dots, *y-axis* on the right), while the nacelle orientation has changed from 61˚ to 57˚ (Fig. 1, black dots). The rotor has turned, probably exclusively during the last 2 minutes, by 0.2 rotation, which corresponds to 72˚.

5

Then, between 17:20 and 17:30, period $P3$, the rotor has started its typical rotation, despite at a speed smaller than usual (2.25 rpm) with blade pitch angles larger than usual, but still close to just a few degrees. The nacelle orientation has changed significantly: from 57° to just a few degrees, where it remains also during period $P4$ (17:30-17:40 UTC). P4 (see Sec. 3.4) has been characterized by a partial rotation of 216° and a different value of the blade pitch angles, which have been again set to 70°. Interestingly, the largest RCS value at horizontal polarization has occurred twice with this configuration (see Sec 4 for more details).

2.3 The polarimetric weather radar measurables (available every 64 ms)

2.3.1 First measurable: radar reflectivity factor at horizontal and vertical polarization

One of the most used quantity measured by weather radar is the so-called "radar reflectivity factor". The backscattered received power, p_r, caused by the hydrometeors and detected by the radar is, in fact, directly proportional to the radar reflectivity factor, z (throughout the manuscript we will simply use reflectivity to refer to it). Since both the received power and the reflectivity span several order of magnitude, they are often expressed using a Log-transformed scale, after having divided the physical quantity by a normalization factor. For linear received power, p_r, the normalization value is typically, $p_0 = 1$ mW. The typical normalization value for the reflectivity is $z_0 = 1$ mm^6/m^3. The dual-polarization radar can simultaneously measure two reflectivity values associated to two orthogonal polarization planes: they will be indicated as z_h and z_v in linear units or Z_h and Z_v after the Log-transformation. As stated, $[z_h] = [z_v] = $ mm^6/m^3, while $[Z_h] = [Z_v] = $ dBz. The upper case P_r indicate the Log-transformed received power, where $[P_r] = $ dBm.

As far as the quantization is concerned, a value of 0.5 dBz has been chosen by the radar manufacturer. At MeteoSwiss, an identical choice has been done regarding the reflectivity resolution of the five C-band radars of the Swiss network; also the formula from converting from 8 bits to physical value is identical. The linear conversion from the 1-byte Digital Number (DN) to Log-transformed radar reflectivity is the following:

$$Z_{dBz} = (DN - 64)/2 \tag{1}$$

However, the maximum recorded value observed operationally in Switzerland (both in the C-band network and with this mobile X-band radar) rarely exceeds 85 dBZ (DN=234); furthermore, a weak echo corresponding to DN=14 (-25 dBZ) can only be detected at a range of 1 km or closer from the X-band radar.

2.3.2 Second measurable: differential reflectivity

The differential reflectivity, Z_{dr}, is an important polarimetric quantity that can be derived by combining the previously described two measurables in a differential manner: it is defined as the Log-transformed ratio between the copolar linear reflectivity measured using horizontal (z_h) and vertical (z_v) polarizations. In formulas:

$$Z_{dr} = 10 \, Log(z_h/z_v) \tag{2}$$

The differential reflectivity is expressed in dB, and a value of 0 dB means that $z_h = z_v$. In practice, Z_{dr} can also be computed as the difference between Z_h and Z_v. The differential reflectivity was introduced by Seliga and Bringi (1976) for a better estimate of rainfall since it contributes to reducing the uncertainty associated with raindrop size distributions. Indeed, the information carried by Z_{dr} is valuable; however, the issue of a proper calibration remains a challenge for successful quantitative precipitation estimation. As far as the quantization is concerned, 256 values (8 bits) are linearly assigned by the manufacturer over an interval that spans 16 dB (from -8 to + 8 dB). We will see in Sec. 3 that, surprisingly, many WT echoes are outside this interval. Consequently, in this study, we abandon such 1/16 dB radiometric resolution and use the poorer 0.5 dB resolution that permits us to derive the value in all circumstances simply as the difference between Z_H and Z_V.

2.3.3 Third measurable: module of the copolar correlation coefficient between horizontal and vertical polarization

An important quantity measured by dual-polarization radars is the correlation between the copolar horizontal and vertical returns, called the copolar correlation coefficient (often referred to as ρ_{HV} , sometimes as ρ_{co}). The copolar correlation coefficient is connected with the differential reflectivity: it is, in fact, related to the dispersion of the differential reflectivity of the 128 instantaneous backscattered signals (with pulse repetition time of 0.5 ms) used to derive each echo every 64 ms. For a detailed and clear description of the interesting and complicated nature of this measurable, the reader may refer to "e06.1", which is the first part of the electronic supplement number six accompanying the book by Fabry (2015). Here it is sufficient to remind that it is the module of the complex correlation coefficient between two orthogonal polarization components and ranges from 0 (no correlation between the two polarizations) to 1 (perfect correlation). If targets within the radar sampling volume were similar, then the time series of signals at horizontal and vertical polarizations would be highly correlated both in amplitude and phase. On the contrary, the greater the variability in shapes of the targets, the smaller will be the value of ρ_{HV}. When many backscatterers are randomly distributed within the sampling volume, the copolar correlation coefficient is considered a measurement of shape diversity. Consequently, the echoes of light rain and drizzle (small and similar spherical drops) are associated with very large values of ρ_{HV}, mostly larger than 0.995; ρ_{HV} values in melting snow are lower (typically between 0.8 and 0.9) and make the melting layer easily distinguishable. If the sampling volume contains a significant number of different targets, such as what happens with ground clutter, ρ_{HV} will decrease considerably. In particular, the range of ρ_{HV} for most ground clutter echoes is between 0.650 and 0.950. Since the most interesting values are very often close to 1, typically a Logarithmic function is used in the quantization process when assigning a DN to the original floating point value of ρ_{HV}. (see for instance eq. 6 in Gabella (2018) for the MeteoSwiss quantization formula that permits increments as small as 0.0001 when close to 1). The X-band radar manufacturer has opted for a linear stretch from 0 to 1, which means equal increments of 0.0039 over the whole interval. This choice is certainly not optimal: for instance, during 5 clear sky days, when 1440 echoes backscattered from the tower at Cimetta have been analyzed (see Sec. 3.5.1 of Gabella, 2018), the present quantization would

only use 4 DNs (from 252 to 255, with mode at DN = 254, which is ρ_{HV} = 0.9961), while MeteoSwiss quantization had DNs ranging from 180 to 251, with mode at DN=233, which is ρ_{HV} = 0.9982.

2.3.4 Fourth measurable: differential phase shift of the copolar signal at horizontal and vertical polarization

Another polarimetric quantity measured by the dual-polarization radar is the differential phase shift, Ψ_{dp}, between the phase of the copolar signal at horizontal and vertical polarization, respectively. Apart from an arbitrary offset value Ψ_0, which can be compensated via software, such difference between the phase of the two orthogonal polarizations arises from two effects:

- A difference in the delay introduced by the scattering of the transmitted wave, known as the backscattering phase shift, δ_{co}.
- A difference in the forward propagation velocity of the two polarizations (reaching the target and coming back to the radar), known as the differential propagation phase, Φ_{dp}.

Keeping in mind Ψ_0, as well as the two important above mentioned terms, then the differential phase delay, Ψ_{dp}, at any given range, r, can be described using a simple formula:

$$\Psi_{dp} = \delta_{co} + \Phi_{dp} + \Psi_0 . \tag{3}$$

At the beginning of the Schaffhausen campaign, the constant Ψ_0, which depends on the radar hardware components and design, has been set to a small positive value close to zero. During dry days, like March 4, 2020, also Φ_{dp} does not vary and can be assumed to be zero. Hence, what is observed when analyzing the dispersion of Ψ_{dp}, is basically the dispersion of the differential backscattering phase delay, δ_{co}. For most ground clutter targets, the dispersion is very large, being its distribution close to a uniform distribution (in this case a standard deviation of $60°\sqrt{3}$ would be expected). On the contrary, in the case of a Bright Scatter (e.g., the tall Cimetta tower presented in Gabella, 2018), the dispersion is small: for instance, the daily standard deviation (288 echoes) of Ψ_{dp} was ~4° in four (out of 5) days analyzed (see Section 3.6 in Gabella, 2018). Something similar could be assumed for a perfectly still WT (zero rotor speed, no changes in nacelle orientation nor in blade pitch angle), as it will be seen in Sec. 3.2.

3 Main results using a 8 s temporal resolution for visualization purposes: from 17:08 UTC to 17:40 UTC

We will show in this descriptive Sec. 3 that for the purpose of visualization and analysis, a small set of three statistical values derived and displayed every 8 s and from the original 64 ms echoes, is adequate and satisfactory in order to characterize the polarimetric radar measurables of the WT. The median has been chosen for a robust representation of the central location of the original 125 echoes available every 8 s. The other two descriptors delimit the extreme boundaries of the 125 echoes: the maximum (green line) and the minimum (blue line).

For a WT, a situation without any movement of the rotor is certainly not a usual one. However, as described in Sec. 2.2, this interesting configuration has already taken place during the first day of the 3-week campaign. As already mentioned in Sec. 2, during the 2-min period $P1$ (17:08-17:10 UTC), rotor speed was assured to be 0 by the WT metadata. This can be seen in Fig. 2, which shows, at the upscaled 8 s resolution, the median (dashed black line), the maximum (green) and minimum (blue) reflectivity values for the horizontal polarization. All the three descriptors are coincident until approximately 17:11 UTC. The backscattered power at horizontal polarization is characterized by a high persistency (Z_H always equal to 56.5 dBz, which is variability smaller than ±0.25 dBz). A similar situation has also characterized the copolar correlation coefficient, which has always been equal to 1 (8 bits always set to 1, namely DN=255), as it can be seen in Fig. 3. For this polarimetric measurable, the three descriptors are coincident until almost 17:14 UTC. This means that ρ_{HV} had same DN for more 5500 consecutive echoes. More details regarding polarimetric signatures during period $P1$ (WT zero rotor speed) are presented in Sec. 3.1.
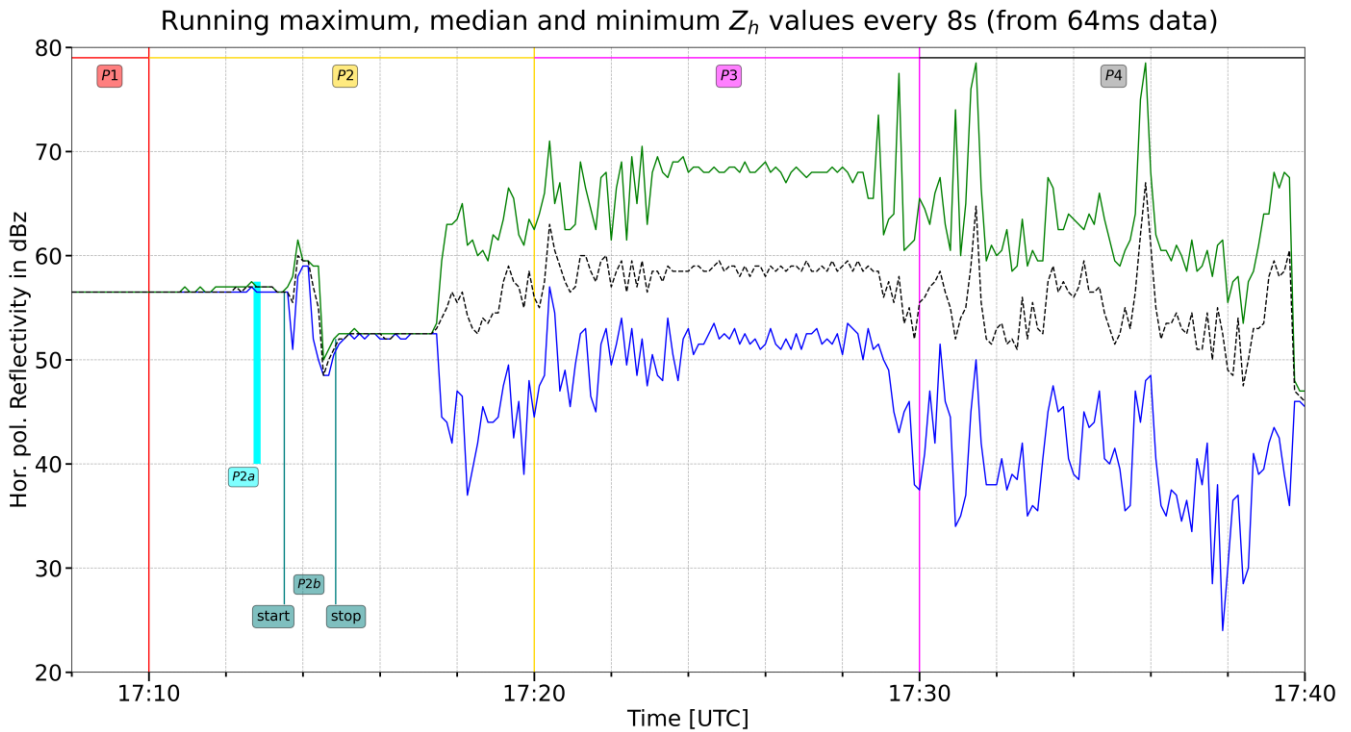

Figure 2. Time line plot of horizontal polarization reflectivity for the 75 m radar gate that contains the wind turbine. The solid lines join 8 s statistical values (median using black, maximum using green, minimum using blue) obtained by using 125 consecutive radar echoes at the original 64 ms resolution. Being the visualization based on 8 s points, the solid lines consist of 240 points that cover 32 minutes (15 points every 2 minutes, which is in correspondence of the vertical grid lines).
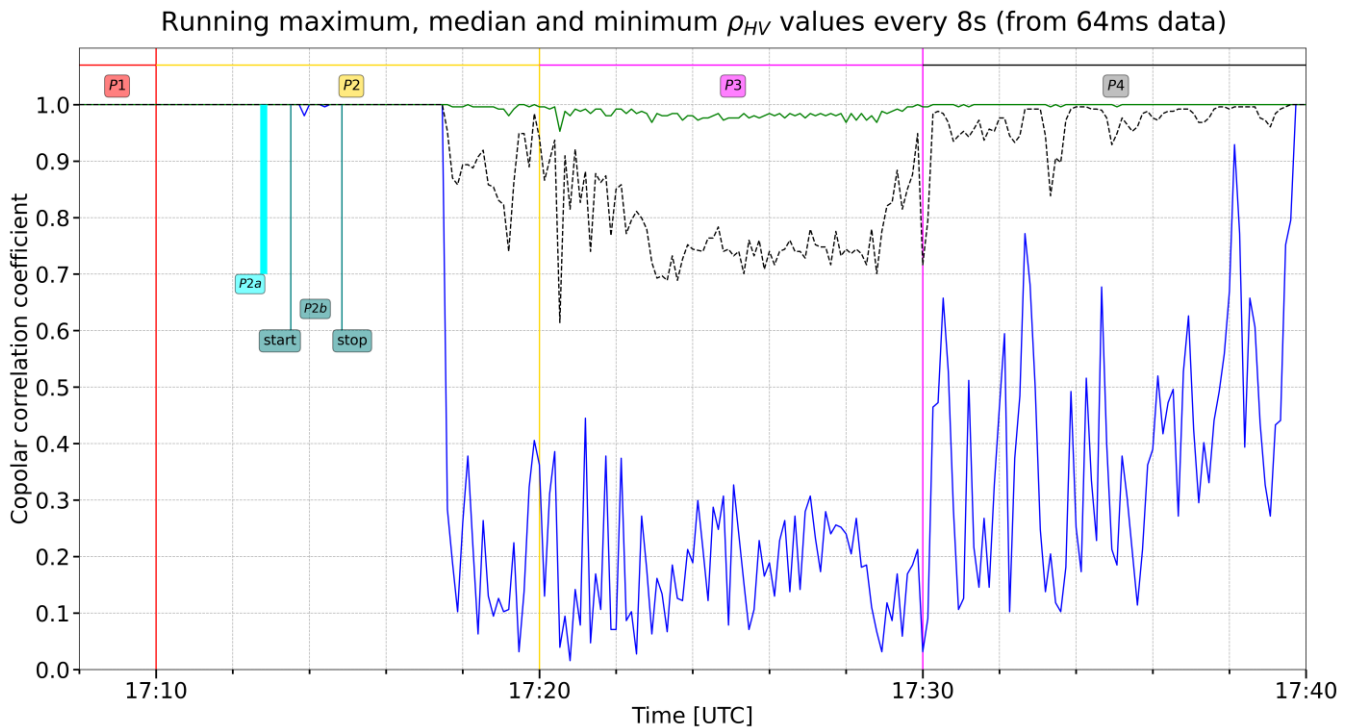
Figure 3. Same as Fig. 2, but for the copolar correlation coefficient, ρ_{HV}. It is interesting to note that the "0 rotor speed condition" read from the WT metadata for the 17:00-17:10 and 17:40-17:50 ten-minute intervals, is probably prolonged also for several minutes after 17:10, as well as anticipated for ~40 s before 17:40 UTC.

3.1 Period *P*1 (17:08-17:10 UTC): 2 min of stare mode radar data (1875 echoes) corresponding to 0 rotor speed

In correspondence of zero rotor speed (as introduced in the beginning of Sec. 3), two polarimetric signatures were constant: the reflectivity at horizontal polarization (Z_H = 56.5 dBz) and the copolar correlation coefficient (ρ_{HV} = 1). The reflectivity at vertical polarization was bounded between 38.5 dBz and 41.5 dBz, as it can be observed in Fig. 4; the mode occurs at 39.0 dBz, the median (mean) value is 40.0 (39.9) dBz. It is interesting to note that at the original (high) temporal resolution of 64 ms, all the reflectivity changes from one echo to the next one, were either 0 dBz or ±0.5dBz. For both polarizations, the significant fact is the stationarity obtained thanks to the stare-mode scanning strategy; hence, the null or quasi-null dispersion is much more interesting than the two random central locations around 56.5 and 40.0 dBz.

For these two minutes, the curve of differential reflectivity (Fig. 5) has no added value, being simply Z_V after a change of sign, plus the constant value of Z_H. From the above-listed values, it is straightforward to derive that median value of Z_{DR}, which is 16.0 dB. When the blades are rotating (rotor speed above 1 rpm), one could expect median (and mode) values not too far from 0 dB. This is in fact the case during most of period *P*3(see Fig. 5 and the thorough description in Sec. 3.3).
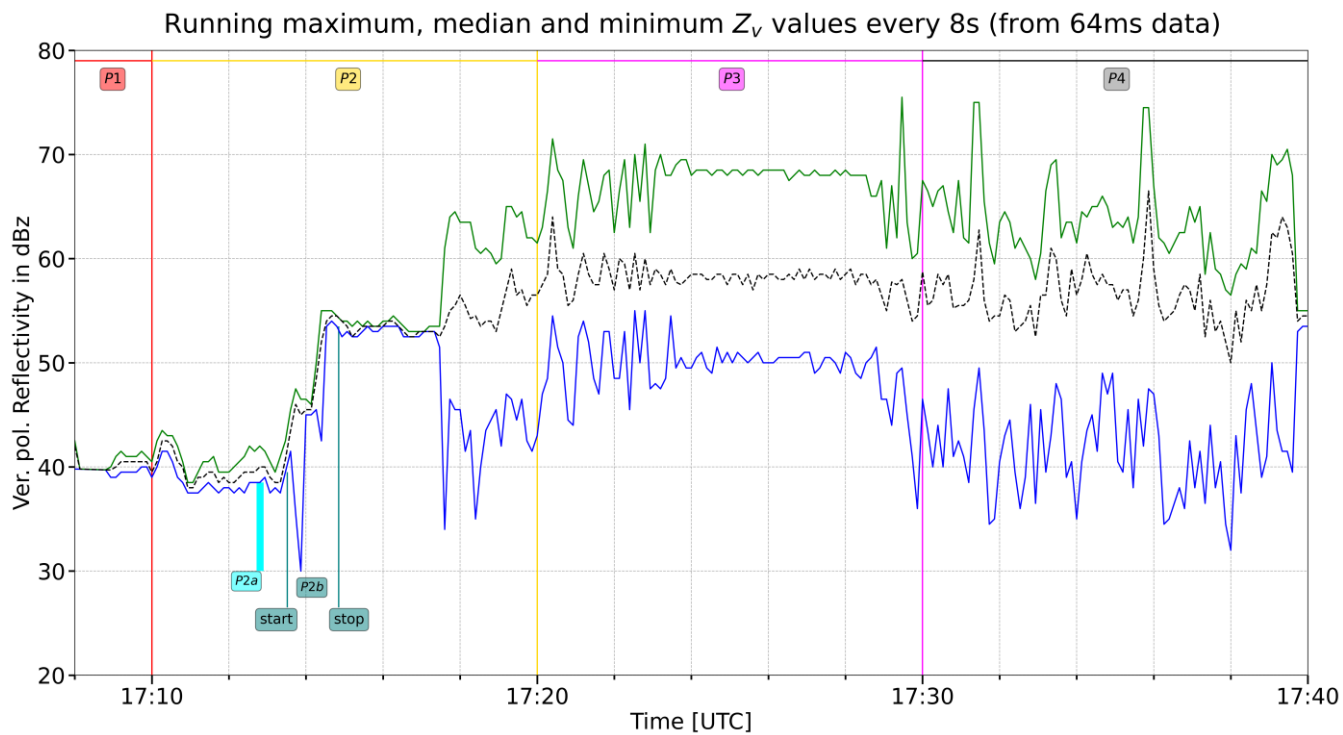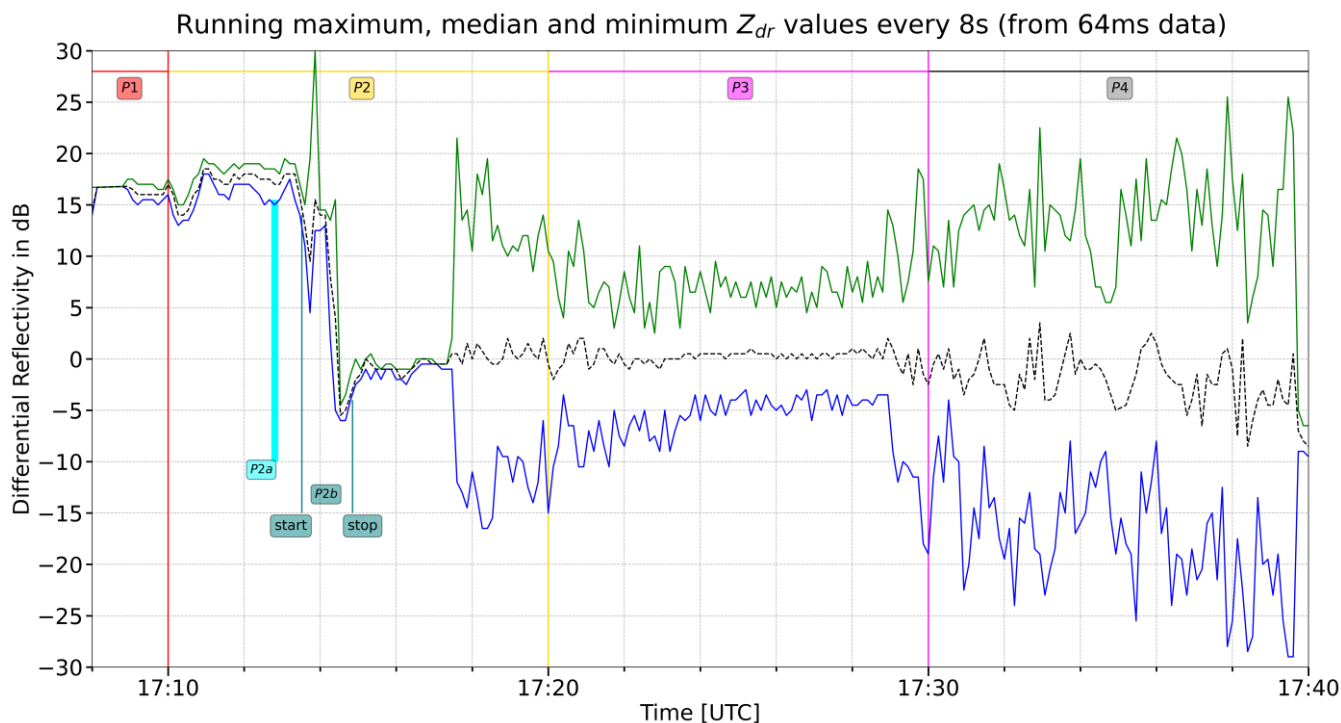
10

Figure 4. Same as Fig. 2, but for the vertical polarization.

Figure 5. Same as Fig. 2, but for the dimensionless differential reflectivity. Most of the 125 echoes between 17:24:00 and 17:24:08 recorded a differential reflectivity value equal to 0 dB ($Z_H = Z_V$). During this 8 s, Z_H (Z_V) has never exceeded Z_V (Z_H) by more than 5 dB (64 ms sampling time, which means 125 echoes). Although the median (and the mode, not shown here) are in general around 0 dB, they are not during the intial and final intervals characterized by 0 rotor speed: our hypothesis is that in steady condition the differential reflectivity depends on the position of the blades as well as their orientation angles.

In case of zero rotor speed, another statistical parameter of particular interest is the dispersion of the differential phase shift, which in the absence of precipitation, was, in fact, coincident with the dispersion of the differential backscattering phase shift, δ_{co}. As shown by Gabella (2021, 2018), small standard deviation of Ψ_{dp} are typical of Bright Scatterers. This is in fact the case for the still WT: the standard deviation during period $P1$ is as small as 3.0˚. On the contrary, a standard deviation of 360˚ divided by the square root of 12 would be expected for randomly distributed Rayleigh backscattering targets.

3.2 Period $P2$ (17:10-17:20 UTC): blade pitch angle changed from 70˚ to 65˚ and small partial rotation

During period $P2$, the average rotor speed was as small as 0.02 rpm. This means that only a partial rotation of 72˚ has occurred during 10 minutes. When has most of the rotation taken place? It seems reasonable to think that it has started around 17:17 UTC, as it could be argued by differences between the 8 s maximum and minimum in Fig. 2 (Z_H), Fig. 4 (Z_V), and Fig. 4 (Z_{dr}). If one were interested to determine with more precision the starting time, he could use the (15.625 Hz) "high-frequency" ρ_{HV} echoes: the constant position of 1 (DN=255) is abandoned exactly at 17:17:17 UTC plus 366 ms. Then ρ_{HV} is characterized by a large dispersion until 20 s before 17:30 UTC, when the rotor speed again slows down considerably and blade pitch angle goes back to 70˚ (see next Sections 3.3 and 3.4).

12

From Fig. 2 and 4, it is possible to see that something has affected both polarizations between 17:13:31 ("start" of the sub-period P2b) and 17:14:51 ("stop" of P2b).The changes during such (80 s long) sub-period P2b have a great impact also on the differential backscattering phase shift (and, in turn, Ψ_{dp}, see eq. 3).

This fact can be seen in Fig. 6, which shows the large changes in the differential phase shift at the original 64 ms sampling time: the changes in the differential phase shift, Ψ_{dp}, are characterized by long sequences of ("high frequency") negative discrete derivative values which bring Ψ_{dp} from the original ("equilibrium") value not far from 0° down to the new ("equilibrium") value of -466°. In fig. 6, the original aliased values (between ±180°) recorded by the radar are shown using blue dots, while the more meaningful de-aliased curve is shown using a solid red line that links all the points.

During 32 s (17:12:59-17:13:31 UTC), just before the starting time of P2b, Ψ_{dp} was oscillating between +11° and +5°, while during the first initial 200 echoes (12.8 s) of P2b, Ψ_{dp} has already monotonically decreased to approximately -20°. Then the slope of the decay starts to increase until a first relative minimum of -369° is reached at echo #355 (the slope has decreased to 0, obviously). Exactly in correspondence of the first, "longer" (9 consecutive 64 ms echoes) and deeper (down to 0.9803, which is DN=250) drop of ρ_{HV}, Ψ_{dp} starts to increase again up to -290°. Then, a rapid decrease down to -466° follows, which is reached around echo #425 (17:13:58.2 s). In the original, aliased data delivered by the radar signal processor, -466° corresponds to a value of -106°. Except a few oscillations between 17:14:13 and 17:14:35, the new "equilibrium" value is kept until 17:17:37, when a new significant change will start.

Adding up, during sup-period P2b (17:13:31-17:14:51), something has caused:

- (large) changes in (Z_V) Z_H that combined cause an extreme variability of Z_{dr}, with a maximum of + 30 dB;
- the consequent Z_{dr} transition from an unexpectedly very large value of ~16 dB to an "expected" value close to 0 dB;
- the transition of Ψ_{dp} (actually, of the differential backscattering phase shift, δ_{co}) from ~0° to -466°.

It could be related to the change in the blade pitch angle from 70° to 65° And/or to the change of the nacelle orientation with respect to the radar (from 61° to 57°). Indeed, one important limitation of the present analysis is due to the very low temporal resolution (sampling time equal to 600 s) of the ancillary data associated to the WT.

Finally, the hypothesis that no change in the WT aspect has happened between 17:13:58 to 17:14:18 UTC is plausible: the standard deviation of Ψ_{dp} is as small as 3.1°: this is typical for a still bright scatterer (see e.g., Sec. 2.3.4 and Sec. 3.6 in Gabella, 2018). Similarly, from 17:14:43 to 17:14:51 UTC, namely the last 8 s in Fig. 6, the standard deviation of $\Psi_{dp}$is 3.6°.
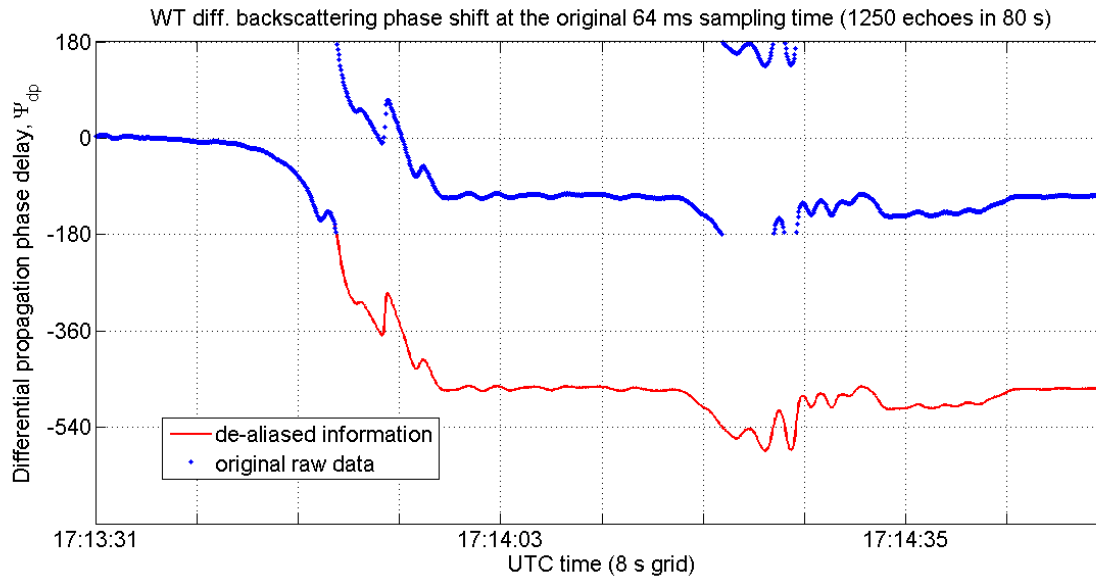
Figure 6. Representation of the variability of the differential phase shift measurable (see Sec. 2.3.4) at the highest available temporal resolution, namely 64 ms. The abscissa spans an interval of exactly 80 s (from 17:13:31 to 17:14:51 UTC); vertical lines on the *x*-axis are every 8 s, which corresponds exactly to 125 echoes. Every 64-ms radar echo (measurable) has been derived by means of 128 pulses transmitted using a Pulse Repetition Frequency of 2000 Hz. The blue dots corresponds to the raw (aliased) data, while the red lines shows the proper evolution of the signal. Since the radar receiver was stable in phase/amplitude and there was no precipitation, changes in the differential phase shift , Ψ_{dp}, can be attributed to changes in the differential backscattering coefficient, δ_{co}.

3.3 Period *P*3 (17:20-17:30 UTC): 22.5 rotor revolutions, blade pitch angle changed from 65° to 15°

During period *P*3, the average 10-min value of r_s is 2.25 rpm, which implies 22.5 revolutions. As far as the blade pitch angle is concerned, it has decreased from 65° to 15°. The whole *P*3 is characterized by heavy fluctuations of ρ_{HV}, which never reaches anymore the value of 1 (green curve in Fig. 3). Regarding the fluctuations of the maximum and minimum reflectivity values of both polarizations (green and blue curves in Fig. 2 and 4), they are smaller between 17:23 and 17:28 UTC; our hypothesis is that during these 5 minutes the rotation was faster than the 10-min average, while before 17:23 UTC and after 17:28 UTC, only a partial, slow rotation was occurring, similar to the one before 17:20 UTC. Thanks to the larger rotor speed, radar estimates are obtained over a larger rotation angle; this leads to a more stable median value of both Z_h and Z_v, as it can be seen in Fig. 2 and 3. During this period with efficient rotor speed for energy production, both polarizations show median reflectivity values around 58 dBz; the median Z_{dr} is around the "neutral" value of 0 dB.

It is particularly interesting that, while the rotor is probably slowing down (precisely at 17:29:31.729), Z_H reaches 77.5 dBz, the 3rd maximum value of the whole campaign. The 3rd maximum value of Z_V can be identified 320 ms earlier (5 echoes back in time). During *P*3, the nacelle orientation changes from 57° to around 10°, where it will remain in the successive 10 minutes (period *P*4, see Sec. 3.4).

14

3.4 Period *P*4 (17:30-17:40 UTC): blade pitch angle back to 70˚ and again partial rotation

During the quasi-steady 17:30-17:40 interval, the average rotor speed was 0.06 rpm; this means that the rotor has turned overall only by 0.6 rotation, which is 216˚. In Sec. 3.2 we had assumed that the partial rotation of 72˚ took place only after 17:17:17 UTC (and before 17:20 UTC); similarly, we here assume that the 216˚ degree rotation was anyhow completed a few tens of seconds before 17:39:41 UTC, when the value of ρ_{HV} became again persistently equal to 1 (see Fig. 3). It is worth noting that the absolute maximum reflectivity value of the whole campaign (78.5 dBz) has been detected in four 64 ms echoes at such very low rotor speed. The four 64 ms echoes belong to only two different 8 s interval (two absolute peaks in the green curve in Fig. 2). In both cases the two 64 ms echoes are consecutive: the first pair is at 17:31:29.167 and 17:31:29.231 UTC, respectively (the corresponding Z_{dr} values are 4.5 and 4.0 dB); the second pair is at 17:35:53.367 and 17:35.431 UTC, respectively (the corresponding Z_{dr} values are 5.5 and 6.0 dB). The nacelle orientation is around 10˚, which is one (among several) 10-deg bin where the absolute maximum of 78.5 dBz has been recorded during the campaign; other orientations involved are around 110˚, 170˚, 260˚ and 340˚, as the reader can see in Fig. 10(a) of Lainer et al. (2021).

It is interesting to note that the slow rotation corresponds again to larger fluctuations of the maximum and minimum reflectivity values of both polarizations, as described in Sec. 3.3 for the first 3 minutes.

Around 17:39:20 UTC, the rotor probably stops its rotation (ρ_{HV} often equal 1):

- Z_v is bounded between 53.5 and 55.5 dBz; smaller than the median of the "energy production" WT mode (for instance, between 17:23 and 17:28 UTC see Sec. 3.3.
- Z_h is bounded between 45.5 and 47.0 dBz, even smaller the median of the 5-min "energy production".
- Consequently, the median differential reflectivity of this 0 rotor speed interval is around -8.0 dB.

4 Discussion

In this preliminary investigation, we have thoroughly analyzed 30 thousands polarimetric echoes acquired in 32 minutes during which the WT rotor has accomplished 23.3 rotations. Thanks to the 10-min ancillary information regarding the WT, we know that the rotor speed was exactly zero during the first 2 minutes. It is also very likely that rotor speed was zero during the last 40 s (from 17:31:40 to 17:32:00 UTC, see Figs. 2-5). If compared to its ordinary rotation conditions, a still WT is much easier to be identified and rejected as clutter. This is something that has been known for a long time. The deep and detailed analysis presented here shows something novel in view of the emerging interest in BS as additional source of information for monitoring dual-polarization weather radars and meteorological applications (e.g., for assessing the path integrated attenuation of a melting hail cell, see Gabella et al. 2021). Indeed, the current polarimetric signatures of the still WT are similar to those of a BS in terms of very small dispersion of both copolar correlation coefficient, ρ_{HV}, and differential phase shift, in addition to the large average and median values of ρ_{HV}. The dispersion is even smaller and the central value even closer to the unity asymptotic limit than for the BS investigated at C-band with a rotating antenna in a previous study. We hypothesize that such an effect

can be due to the special stare mode antenna scan program: all the 128 averaged pulses refer to an antenna beam axis that is pointing in the same geometrical direction. Residual sources of variability are then only fluctuations of the tropospheric refraction index and small movements of the blade tips. Similarly, for a still WT, the dispersion of both dual-pol. reflectivities and differential reflectivity is also much smaller than any other moving conditions.

Furthermore, with this preliminary study, it was possible to identify other WT configurations, which are causing quite different polarimetric signatures with respect to the simple still WT condition, labelled with a) here below :

a) Zero rotor speed and probably no change in either blade pitch angle or nacelle orientation. Surely from 17:08 to 17:10 UTC, period $P1$ (see Figures 2-5 and Sec. 3.1); however, this configuration has probably been lasting until 17:13:31 UTC (see Sec. 3.2). Our hypothesis is that it has happened again in other two intervals: between 17:14:41 UTC ad 17:17:37 UTC (see Sec. 3.2) and during the last 40 s before 17:40 UTC (see Sec. 3.4), as it can be deduced from Figures 2 to 5.

b) Another distinctive (and probably rare) configuration is the one described in the central part of Sec. 3.2 as well as in Fig. 6 and that has occurred between 17:13:31 and 17:14:41 UTC, namely the sub-period $P2b$, see Fig. 2. It could have been caused by a change in the blade pitch angle, while the rotor speed was still 0. This is just a plausible hypothesis. Whatever the reason could be, the changes in the differential backscattering coefficient, δ_{co}, is quite significant (see Fig. 6).

c) Then the most usual configuration comes, which is the one of energy production under sufficient wind conditions. We think that it has been lasting approximately 6 minutes (say from 17:23 to 17:28 UTC) during which most of the 22.5 rotations of period $P3$ has occurred.

d) Finally a configuration that is associated to large variability of the parametric signatures (from 17:17:37 UTC to approximately 17:23 UTC and, most of all, from approximately 17:28 UTC to 17:39:20 UTC, see Sec. 3.4).

Regarding a), we conclude that when the rotor speed is zero, the WT signatures are similar to those of a Bright Scatterer: we have observed, in fact, a good stability and small dispersion of the polarimetric variables; the situation is even better than what have been observed with a rotating antenna ($18°s^{-1}$) by Gabella (2018) using the metallic tower on Cimetta at 18 km range from the Monte Lema C-band radar. The even larger stability and small dispersion in the present campaign is due to the stare mode antenna of the X-band radar. A very small dispersion of the polarimetric variables is also observed from 17:10:00 UTC to 17:17:40 UTC and from 17:39:40 to 17:40:00 UTC interval. Our guess is that in both cases the rotor speed was equal to zero, which is exactly the status of the previous (17:00-17:10 UTC) and following (17:40-17:50 UTC) 10-min interval. A preliminary analysis of a different case (about 90 minutes of radar data collected on March 19, 2021) not included in the present paper has shown also ρ_{HV} values always equal to 1. For this case, the three operational parameters of the WT (nacelle orientation, pitch angle of the blades, rotor speed) heavily affecting the backscattering signatures did not change: in particular, rotor speed was always zero in the interval of interest.

16

Regarding b), let us focus again on the 1000 radar polarimetric values acquired in 64 s of the sub-period $P2b$ (see Fig. 2), namely from 17:13:31 UTC to 17:14:35 UTC: one can easily see large changes in both horizontal (Fig. 2) and vertical (Fig. 4) polarization reflectivity (and consequently extreme variability of Z_{dr} reaching an extreme maximum of +30 dB and a minimum

410   of +4.5 dB, Fig. 5); transition of Z_{dr} from a large value of +16 dB to approximately 0 dB; transition of the differential phase shift, Ψ_{dp}, from around ~0˚ to -466˚, probably caused by an overall change of 466˚ of the differential backscattering phase shift. What can be the cause of such simultaneous large changes in Z_{dr} and Ψ_{dp}? It could be a change in the blade pitch and/or nacelle orientation. Was there also a small movement of the rotor? It is hard, if not impossible, to find an answer to such questions with the present data. For future campaigns, it is obvious to recommend a much better (smaller) sampling time regarding the

415   WT status and wind information: ideally, from the current 600 s down to 1 s or less. Another obvious recommendation is related to the quantization of ρ_{HV}: either using two bytes or a Log-transformation, like for instance the operational one used at MeteoSwiss (see Eq. 6 in Gabella, 2018).

There are two other facts worth mentioning: the first one is a sort of "intrinsic" inverse correlation between the dispersion and the central value of the copolar correlation coefficient among many consecutive 64 ms echoes . When ρ_{HV} is close to the

420   asymptotic value of 1, then the changes among successive echoes tend to be very small (see Fig. 3, from 17:30 to 17:40 UTC, partial rotor rotation of 216˚ in ten minutes). As stated, when the rotor is not moving, blade pitch angle and orientation not changing, then ρ_{HV} is consistently and constantly equal to 1; this fact has been confirmed by analyzing 86250 high temporal resolution echoes on March 19, 2020.

The second fact is an occasional, short lasting, quite surprising correlation between the differential phase shift (4th measurable,

425   see Sec. 2.3.4) and the differential reflectivity (2nd measurable, see Sec. 2.3.2) associated to a sort of cyclo-stationarity (although during very short intervals): this fact can be seen, for instance, during the 8.96 s (140 echoes) displayed in Fig. 7 during which approximately 5 periodic cycles of the two polarimetric measurable took place. In Fig. 7, the vertical lines are every 28 echoes (1.792 s); obviously, our intention is not to claim that the period is exactly 1.792 s, since 1.728 s (27 echoes) is certainly another reasonable estimate.
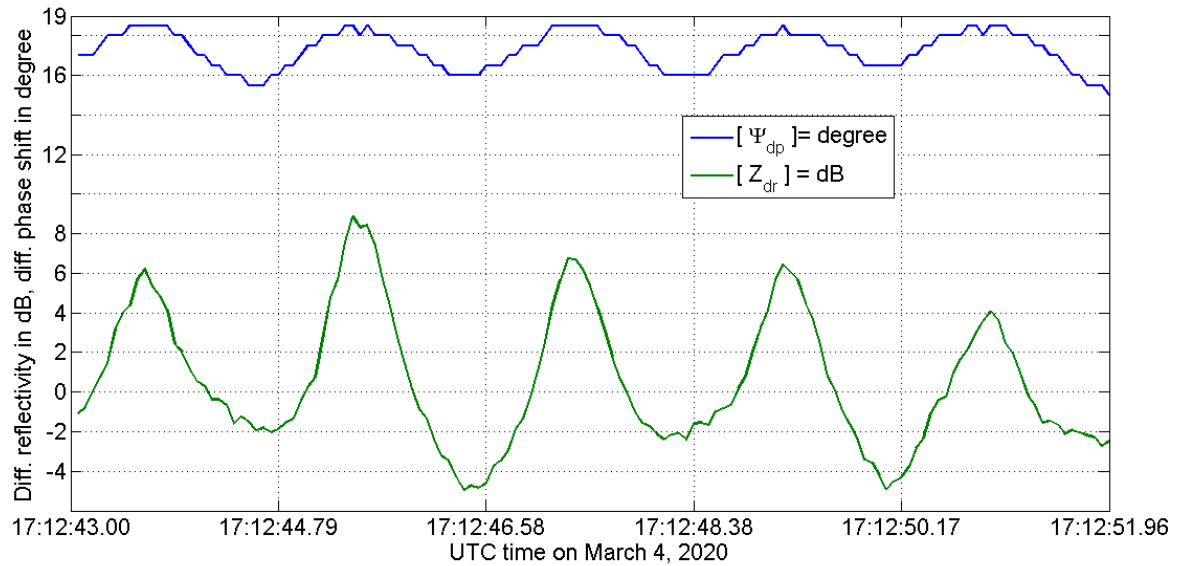
430

Figure 7. An example of quasi-cycle-stationarity of both the differential reflectivity in dB (green line) and the differential phase shift in degree (blue line) at the highest available temporal resolution, namely 64 ms. The abscissa spans an interval of exactly 8.96 s, which corresponds exactly to 140 echoes. Vertical lines are every 1.792 s, which is 28 consecutive echoes.

435 We think it is interesting to emphasize that there must be something WT-related with a period of ~1.7-1.8 s, which is reflected in both the (differential) phase and (differential, squared) amplitude of the polarimetric signals received by the radar.

5 Summary, conclusions and outlook

This technical note has extended the analysis and investigation by Lainer at al. (2021) in two directions:

1. To complement the statistics of horizontal polarization radar reflectivity factor, with those corresponding to other
440   polarimetric measurables: the copolar correlation coefficient, ρ_{HV}; the vertical polarization reflectivity factor; the differential reflectivity, Z_{dr}; and the differential phase shift, Ψ_{dp}, between the phases of the copolar signals at horizontal and vertical polarization.

2. To investigate their variability at the best available temporal resolution (sampling time as short as 64 ms), despite the precious and valuable ancillary data related to the wind turbine status being available only every 600 s.

445 We have tackled the challenging sampling time (600 s vs 0.064 s) problem by starting with an interval that was characterized by zero rotor speed (still wind turbine). In such distinctive case of still WT we have observed that

- ρ_{HV} is perfectly stable and always equal to 1 (DN = 255).

18

- 38.5 dBz $\leq Z_v \leq 41.5$ dBz, i.e. only 7 Digital Numbers are used; the standard deviation is as small as 0.725 dBz. By way of example, note that from 4:00 to 4:10 UTC on March 19, it was 53.0 dBz $\leq Z_v \leq 54.5$ dBz. Hence, Z_v has shown a smaller variability and was constant during several seconds.

- Since Z_h is always equal to 56.5 dBz (see Sec. 3.1), the temporal variability of Z_{dr} is identical to Z_v (just with the opposite sign, obviously). Similarly, from 4:00 to 4:10 UTC on March 19, it was 54.5 dBz $\leq Z_h \leq 55.5$ dBz. Furthermore, Z_h was constant during several minutes.

- For both Z_h and Z_v, the interesting fact, is the very small range of variability of the still WT, which acts as a Bright Scatterer. As expected, such extreme stationarity of the backscattered signal by a BS cannot be obtained with a rotating antenna (see, e.g. Gabella, 2018).

- $4° \leq \Psi_{dp} \leq 40°$ during a 2-minute interval, with periodic oscillation of approximately $\pm 3°$ in a bit less than 2 s; the standard deviation is as small as $2.9°$.

The large difference in sampling time (64 ms vs 600 s) poses certainly a challenge to future analyses of the 3-week valuable campaign in March 2020. Nevertheless, we plan to extend this (32-minute) analysis (based on thirty thousand polarimetric measurables) to a distinctive day (March 19, 2020), which is characterized by several 10-min intervals with zero rotor speed. As stated, a preliminary analysis during 92 minutes has shown similar results: ρ_{HV} always equal to 1, small dispersion of the radar reflectivity factors.

The "prevailing in time", stare mode acquisition of the 2020 campaign has been proved to be highly beneficial for a better characterization of the polarimetric signatures of the wind turbine, especially when it is still (or quasi-still). The results from previous studies (Lainer et al. 2021) are, in fact, confirmed: the rotor speed is a key information in order to predict the values and the variability of backscattered power and phase of horizontal and vertical polarizations. Another important parameter is the rotor blade pitch angle, which is probably changed in a relatively short time, much shorter than the 600 s sampling time of the turbine data obtained so far. At the moment, more difficult to assess is the dependence on the nacelle orientation. Surely, we are just at the beginning of the fascinating task of deriving spectral and polarimetric signatures of wind turbines from the point of view of a weather radar, keeping in mind that the special results of the present experiment where possible thanks to the stare mode scan strategy. An operational radar with a rotating antenna will retrieve variances of the polarimetric signatures that are affected by both changes: those of the WT (blades rotation) and those of the radiation pattern (antenna rotation)

stimulated a fast, preliminary look at additional high temporal resolution radar data associated to other still WT conditions of the campaign (March 19). Reviewer 1 has also provided an interesting and illustrative interpretation scheme based on 9 points, which we recommend to the readers: we highly appreciate the fact that Reviews are public in this journal, so that they will be available to all.

485

Author contributions. Conceptualization, data analysis and investigation, first draft preparation, writing and revision: MG. ML has drawn the revised version of Figs. 2-5. Writing-review, discussions, interpretation and editing JG, ML, DW and MG. All authors have read and agreed to the submitted revised version of the manuscript.

490

References

495   Angulo, I., de la Vega, D., Cascon, I., Canizo, J.,Wu, Y., Guerra, D., and Angueira, P.: Impact analysis of wind farms on telecommunication services, Renewable and Sustainable Energy Reviews, 32, 84–99, https://doi.org/ 10.1016/j.rser.2013.12.055, 2014.

Angulo, I., Grande, O., Jenn, D., Guerra, D., and de la Vega, D.: Estimating reflectivity values from wind turbines for analyzing the potential impact on weather radar services, Atmos. Meas. Tech., 8, 2183–2193, https://doi.org/10.5194/amt-
500   8-2183-2015, 2015.

Bredemeyer, J., Schubert, K., Werner, J., Schrader, T., and Mihalachi, M.: Comparison of principles for measuring the reflectivity values from wind turbines, in: 2019 20th International Radar Symposium (IRS), pp. 1–10, https://doi.org/ 10.23919/IRS.2019.8768171, 2019.

Brindley, G.: Financing and investment trends: The European wind industry in 2021, Technical report available from
505   Wind EUROPE, Brussels, Belgium, p. 1-40, 2022

Cuadra, L., Ocampo-Estrella, I., Alexandre, E., and Salcedo-Sanz, S.: A study on the impact of easements in the deployment of wind farms near airport facilities, Renew. Energ., 135, 566–588, https://doi.org/10.1016/j.renene.2018.12.038, 2019.

de la Vega, D., Jenn, D., Angulo, I., and Guerra, D.: Simplified characterization of Radar Cross Section of wind
510   turbines in the air surveillance radars band, in: 2016 10th European Conference on Antennas and Propagation (EuCAP), Curran Associates, Inc, Red Hook, NY, USA, pp. 1–5, ISBN 978-88-907018-6-3, 2016.

Douvenot, R., Claudepierre, L., Chabory, A., and Morlaas, C.: Probabilistic VOR error due to several scatterers — Application to wind farms, 2017 11th European Conference on Antennas and Propagation (EUCAP), pp. 2057-2060, doi: 10.23919/EuCAP.2017.7928653, 2017.

515 Fabry, F. Radar Meteorology: Principles and Practice, 1st ed.; Cambridge University Press: Cambridge, UK, 2015; 256p, ISBN 978-1-107-07046-2.

Gabella, M.; Perona, G. Simulation of the Orographic Influence on Weather Radar Using a Geometric-Optics Approach. *J. Atmos. Oceanic Technol. 15*, 1485 – 1494, 1998.

Gabella, M.; Notarpietro, R.; Turso, S.; Perona, G. Simulated and measured X-band radar reflectivity of land in 520 mountainous terrain using a fan-beam antenna', International Journal of Remote Sensing, *29*, 2869 – 2878, 2008.

Gabella, M.: On the Use of Bright Scatterers for Monitoring Doppler, Dual-Polarization Weather Radars. Remote Sens. 10, 1007, https://doi.org/10.3390/rs10071007, 2018.

Gabella, M.,: On the Spectral and Polarimetric Signatures of a Bright Scatterer before and after Hardware Replacement. Remote Sens. 13, 919, https://doi.org/10.3390/rs13050919, 2021.

525 Gabella, M., Sartori, M., Boscacci, M., and Germann, U.: Electrical and Sun calibration: what to trust when they disagree?, 3rd Calibration and Monitoring workshop WXRCALMON 2021, 17-19 November 2021, Toulouse, France, https://www.meteo.fr/cic/meetings/2021/wxrcalmon/

Germann, U.; Boscacci, M.; Clementi, L.; Gabella, M.; Hering, A.; Sartori, M.; Sideris, I.V.; Calpini, B. Weather Radar in Complex Orography. Remote Sens*. 14*, 503. https://doi.org/10.3390/rs14030503, 2022.

530 Gallardo-Hernando, B., Muñoz-Ferreras, J. M., Pérez-Martínez, F., and Aguado-Encabo, F.: Wind turbine clutter observations and theoretical validation for meteorological radar applications, IET Radar, Sonar & Navigation, 5, 111–117, https://doi.org/ 10.1049/iet-rsn.2009.0296, 2011.

Hall, W., Rico-Ramirez, M. A., Kraemer S.: Offshore wind turbine clutter characteristics and identification in operational C-band weather radar measurements, Q. J. Royal Met. Soc., 143, 720-730, doi:10.1002/qj.2959, 2017.

535 Hood, K., Torres, S., and Palmer, R.: Automatic Detection of Wind Turbine Clutter for Weather Radars, J. Atmos. Ocean. Tech., 27, 1868–1880, https://doi.org/10.1175/2010JTECHA1437.1, 2010

Lainer, M., Figueras i Ventura, J., Schauwecker, Z., Gabella, M., F.-Bolaños, M., Pauli, R., and Grazioli, J.: Insights into wind turbine reflectivity and radar cross-section (RCS) and their variability using X-band weather radar observations, Atmos. Meas. Tech., 14, 3541–3560, https://doi.org/10.5194/amt-14-3541-2021, 2021.

540 Interactive comment on Atmos. Meas. Tech. Discuss., https://amt.copernicus.org/preprints/amt-2020-384/amt-2020-384-RC1.pdf): doi:10.5194/amt-2020-384-RC1, 2020.

Kent, B. M. et al.: Dynamic Radar Cross Section and Radar Doppler Measurements of Commercial General Electric Windmill Power Turbines Part 1: Predicted and Measured Radar Signatures, IEEE Antennas and Propagation Magazine, vol. 50, no. 2, pp. 211-219, doi: 10.1109/MAP.2008.4562424, 2008.

21

545   Kong, F., Zhang, Y., Palmer, R., and Bai, Y.: Wind Turbine radar signature characterization by laboratory measurements, in: 2011 IEEE RadarCon (RADAR), pp. 162–166, https://doi.org/10.1109/RADAR.2011.5960520, 2011.

Lepetit, T., Simon, J., Petex, J. ., Cheraly, A., and Marcellin, J. .: Radar cross-section of a wind turbine: application to weather radars, in: 580 2019 13th European Conference on Antennas and Propagation (EuCAP), pp. 1–3, 2019.

Morlaas, C., Fares, M., and Souny, B.: Wind turbine effects on VOR system performance, IEEE Transactions on

550   Aerospace and Electronic Systems, vol. 44, no. 4, pp. 1464-1476, doi: 10.1109/TAES.2008.4667722, 2008.

Muñoz-Ferreras, J., Peng, Z., Tang, Y., Gómez-García, R., Liang, D., and Li, C.: Short-Range Doppler-Radar Signatures from Industrial Wind Turbines: Theory, Simulations, and Measurements, IEEE Transactions on Instrumentation and Measurement, 65, 2108–2119, https://doi.org/10.1109/TIM.2016.2573058, 2016.

Norin, L.: A quantitative analysis of the impact of wind turbines on operational Doppler weather radar data, Atmos.

555   Meas. Tech., 8, 593–609, https://doi.org/10.5194/amt-8-593-2015, 2015.

Norin, L.: Wind turbine impact on operational weather radar I/Q data: characterisation and filtering, Atmos. Meas. Tech., 10, 1739–1753, https://doi.org/10.5194/amt-10-1739-2017, 2017.

Probert-Jones, J. R.: The radar equation in meteorology, Q. J. Roy. Meteorol. Soc., 88, 485–495, https://doi.org/10.1002/qj.49708837810, 1962.

560   Rinehart, R. E.: On the Use of Ground Return Targets for Radar Reflectivity Factor Calibration Checks. Journal of Applied Meteorology, 17, 1342–1350, 1978.

Seliga, T.; Bringi, V. Potential use of radar differential reflectivity measurements at orthogonal polarizations for measuring precipitation. J. Appl. Meteor. 1976, 15, 69–76